Electronic Supplementary Information

All-Solid-State Flexible Planar Lithium Ion Micro-Capacitors

Shuanghao Zheng,[abc] Jiaming Ma,[d] Zhong-Shuai Wu,*[a] Feng Zhou,[a] Yan-Bing He,*[d] Feiyu Kang,[de] Hui-Ming Cheng[ef] and Xinhe Bao[ab]

[a] Dalian National Laboratory for Clean Energy, Dalian Institute of Chemical Physics, Chinese Academy of Sciences, 457 Zhongshan Road, Dalian 116023, China. E-mail: wuzs@dicp.ac.cn

[b] State Key Laboratory of Catalysis, Dalian Institute of Chemical Physics, Chinese Academy of Sciences, 457 Zhongshan Road, Dalian 116023, China

[c] University of Chinese Academy of Sciences, 19 A Yuquan Rd, Shijingshan District, Beijing, 100049, China

[d] Engineering Laboratory for the Next Generation Power and Energy Storage Batteries, Graduate School at Shenzhen, Tsinghua University, Shenzhen 518055, China. E-mail: he.yanbing@sz.tsinghua.edu.cn

[e] Tsinghua-Berkeley Shenzhen Institute (TBSI), Tsinghua University, 1001 Xueyuan Road, Shenzhen 518055, China

[f] Shenyang National Laboratory for Materials Science, Institute of Metal Research, Chinese Academy of Sciences, 72 Wenhua Road, Shenyang 110016, China

Methods

Preparation of LTO nanospheres. LTO nanospheres were fabricated according to our previous procedure.[1] Typically, titanium nitride (0.25 g) in 28 mL deionized water was mixed with 16 mL hydrogen dioxide (30%), and then 6 mL ammonia solution (25-28%) was added in the above mixed dispersion under continuous stirring for 30 min. Afterwards, 50 mL water and 100 mL ethanol were added into the above solution for further hydrolysis of peroxo-titanium complex. Successively, $LiOH \cdot H_2O$ (0.14 g) and polyvinyl pyrrolidone (100 mg) were uniformly mixed with the resulting precursor solution, and dried at 80 ^oC. Thus, the collected white powder was annealed at 750 ^oC for 7 h in inert atmosphere. Finally, LTO nanospheres were obtained.

Preparation of AG. AG was prepared from graphene oxide with the activation of KOH.[2, 3] Briefly, 50 mL graphene oxide (10 mg mL^{-1}) was uniformly mixed with 3 g KOH stirring for 2 h, and then the resultant dispersion was dried at 100 ^oC to evaporate the solvent until the black gray slurry was obtained. Subsequently, the slurry was heated at 110 ^oC for 30 min to remove the residual water at N_2 gas with a flow rate of 300 mL min^{-1}, and then kept at 700 ^oC for 1 h for activation. After the powder was completely washed with 1 M HCl and deionized water to fully remove residual salt, AG powder was achieved.

Fabrication of all-solid-state LTO//AG-LIMCs. First, the stable EG ink of 3 mL (0.1 mg mL^{-1} in ethanol) was filtrated on a nylon membrane (0.22 μm in pore size), with help of a customized interdigital mask (8 fingers, 14 mm in length, 1 mm in width, and 0.5 mm width of interspacing). Subsequently, the negative-electrode ink of

LTO and EG (0.5 mg mL^{-1} in ethanol, LTO: EG mass ratio of 9:1) was added on one side (four fingers) of the interdigital mask, and the positive-electrode solution of AG and EG (0.25 mg mL^{-1} in ethanol, AG:EG mass ratio of 9:1) was also filtrated on the other side (four fingers) of the mask. Successively, 2 mL EG ink (0.02 mg mL^{-1}) was filtered on the top of LTO and AG active electrodes. After removing the mask and drying at 60 ^{o}C for 12 h, the planar interdigital patterns of film microelectrodes were obtained. Afterwards, ionogel electrolyte of LiTFSI-P_{14}TFSI-PVDF-HFP was carefully brush-coated on the fingers and solidified. Finally, all-solid-state planar LTO//AG-LIMCs were achieved after Kapton tape package. For comparison, AG//AG-MSCs using AG as active materials for both electrodes were also fabricated based on the same thick film of positive electrode of LTO//AG-LIMCs, while other steps kept the same as the latter.

Ionogel electrolyte. LiTFSI-P_{14}TFSI-PVDF-HFP was prepared via the following steps. LiTFSI was first dissolved into P_{14}TFSI to form the transparent solution of 1 M LiTFSI-P_{14}TFSI. Then, 0.2 g PVDF-HFP was added into acetone under continuous stirring for 4 h to form uniform clear dispersion. Subsequently, 2.5 g LiTFSI-P_{14}TFSI solution was slowly mixed with the above PVDF-HFP dispersion. Finally, ionogel electrolyte of LiTFSI-P_{14}TFSI-PVDF-HFP was attained.

Materials Characterizations. The morphology and structures of LTO nanospheres, AG, EG, and the fabricated electrodes were examined using SEM (JSM-7800F), HRTEM (JEM-2100), XRD (X`pert Pro), nitrogen adsorption/desorption isotherms (Micromeritcs Tristar 3020 analyzer), and four-point probe equipment (RTS-9).

Thermogravimetric analysis (TGA, STA 449 F3) was used for thermal stability of ionogel electrolyte. The ionic conductivity (σ) of ionogel electrolyte as a function of temperature was tested by EIS at the frequency from 100 kHz to 0.1 Hz with an AC amplitude of 5 mV, based on a cell of stainless steel/ ionogel electrolyte /stainless steel. The value of σ was evaluated by the equation： σ = L/(R*S), where *L* is the length of ionogel electrolyte film, *R* is ESR from EIS, *S* is the geometric area of ionogel electrolyte film and electrode interface.

Electrochemical Measurement. The electrochemical performances were performed by electrochemical workstation (CHI760E). CV curves were measured with scan rates from 2 to 20 mV s^{-1}. GCD profiles were tested at different current densities ranging from 0.02 to 1 mA cm^{-2}. EIS were recorded in the frequency range from 100 kHz to 0.01 Hz with the ac amplitude of 5 mV. Cycling stability was carried out on LAND CT2001A battery tester at the current density of 0.4 or 1.0 mA cm^{-2}. High-temperature performance measurement at 50 ^{o}C and 80 ^{o}C of LTO//AG-LIMCs was kept at the tested temperature for 1 h until equilibration.

Calculation

The capacitance of the fabricated planar interdigital microdevices was calculated by the discharged curves of GCD via the following equation (1):

$$C = \frac{It}{\Delta V} \qquad (1)$$

Where C is the evaluated capacitance value, *I* (A) is the discharge current, t (s) is discharge time, and ΔV (V) is potential difference of GCD profiles.

Areal and volumetric capacitances of a device were evaluated according to the

area and volume of the device by the following formula (2) and (3):

$$C_{device}^{areal} = C / A_{device} \quad (2)$$

$$C_{device}^{volumetric} = C / V_{device} \quad (3)$$

Where A_{device} (cm^2) and V_{device} (cm^3) refer to the area and volume of the device, respectively. $C_{\text{device}}^{areal}$(F cm^{-2}) and $C_{device}^{volumetric}$(F cm^{-3}) are labeled as areal capacitance and volumetric capacitance of the device, respectively. The areal and volume of the device refer to all the electrode fingers.

The volumetric energy density and power density of a device were obtained from the following relationships (4) to (6):

$$P = \frac{\Delta UI}{V_{device}} \quad (4)$$

$$E = Pt \quad (5)$$

$$\Delta U = \frac{1}{2} \times (U_{\max} + U_{\min}) \quad (6)$$

where P is the volumetric power density (W cm^{-3}) and E is the volumetric energy density (Wh cm^{-3}), and $U_{\max}$ and $U_{\min}$ are the high and low potential of GCD profiles, respectively.

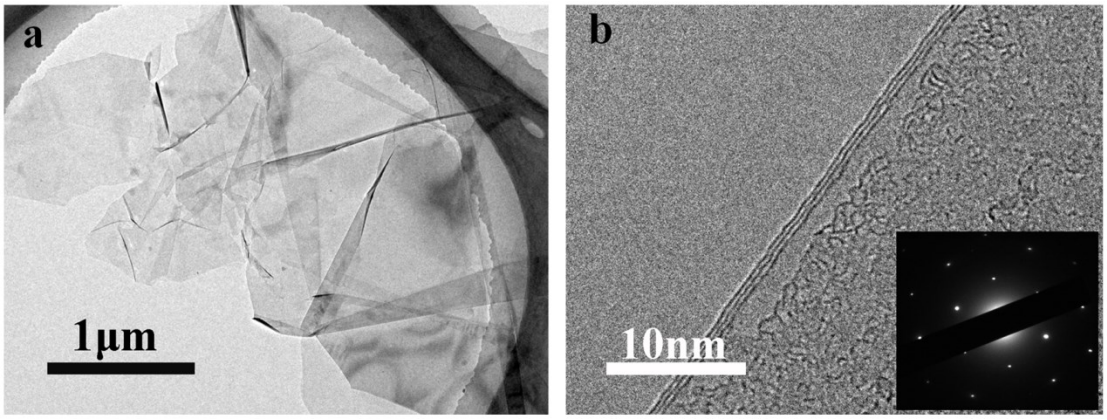

Fig. S1 Morphology and structure of EG nanosheets. (a) TEM image, showing the flat and uniform morphology. (b) HRTEM image, showing a trible-layer structure. Inset is the SAED pattern, indicative of high-quality EG.

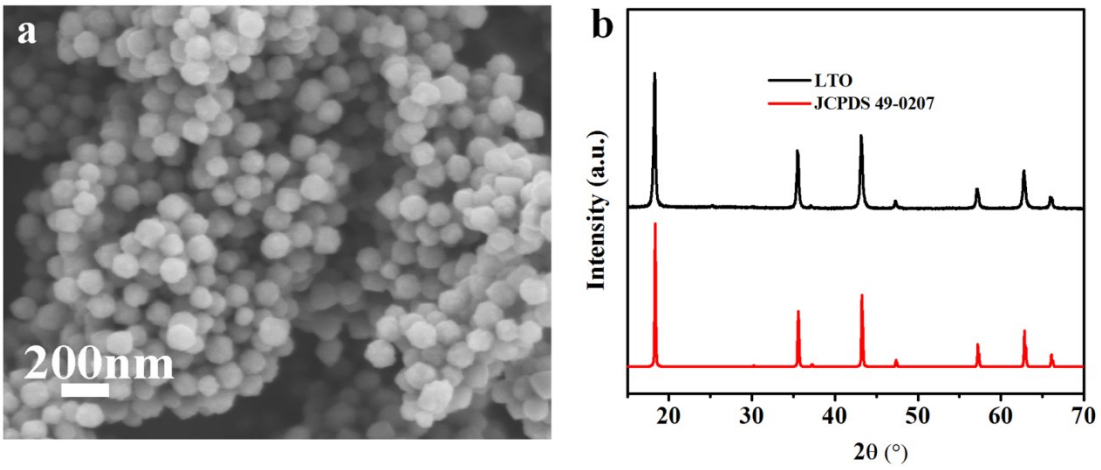

Fig. S2 Morphology and structure of LTO nanospheres. (a) SEM image, showing LTO nanospheres with the average size of ~120 nm. (b) XRD pattern of LTO nanospheres, exhibiting all characteristic diffraction peaks, which are in good agreement with the standard card of JCPDS 49-0207.

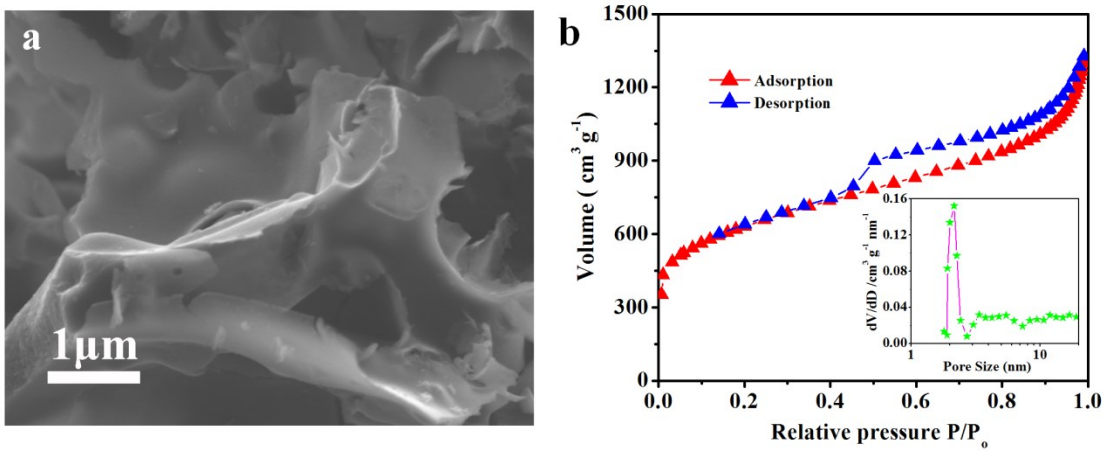

Fig. S3 Morphology and structure of nanoporous AG. (a) SEM image. (b) Nitrogen adsorption and desorption isotherm of AG. Inset is the pore-size distribution profile, showing a narrow mesoporous distribution of 2.6 nm.

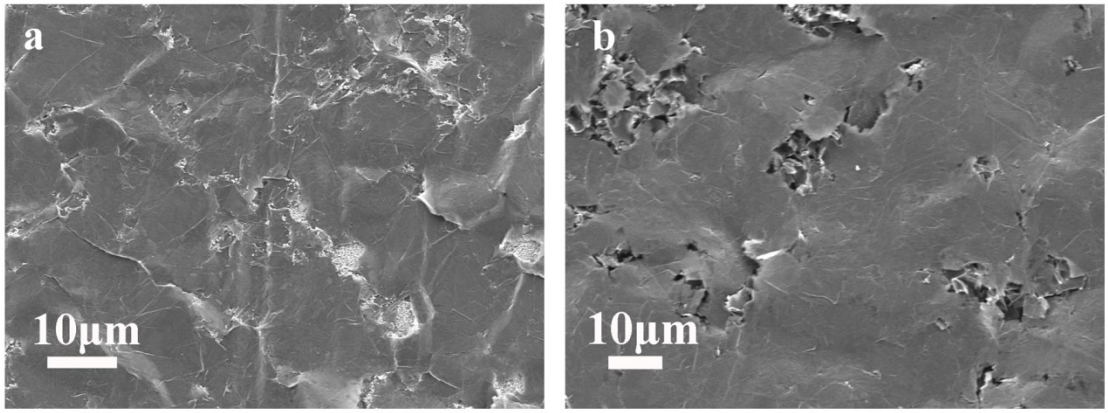

Fig. S4 Top-view morphology of LTO//AG electrodes. (a,b) Top-view SEM images of LTO electrode (a) and AG electrode (b), showing the large-area uniformity and flat morphology of LTO//AG electrodes.

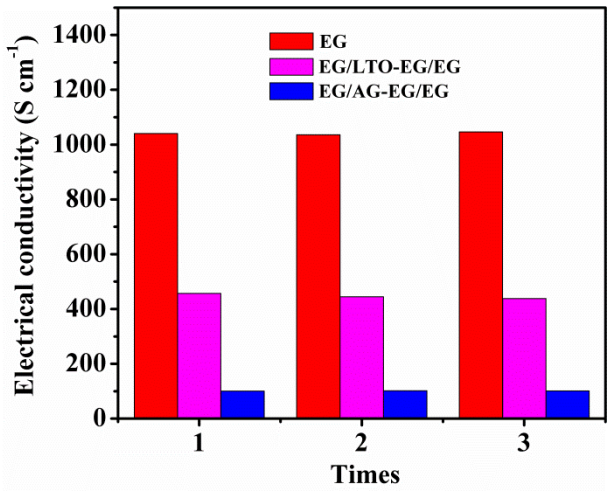

Fig. S5 Electrical conductivity of the fabricated EG layer, anode and cathode. The conductivity of the EG layer, anode and cathode is 1041, 447 and 101 S cm^{-1}, respectively.

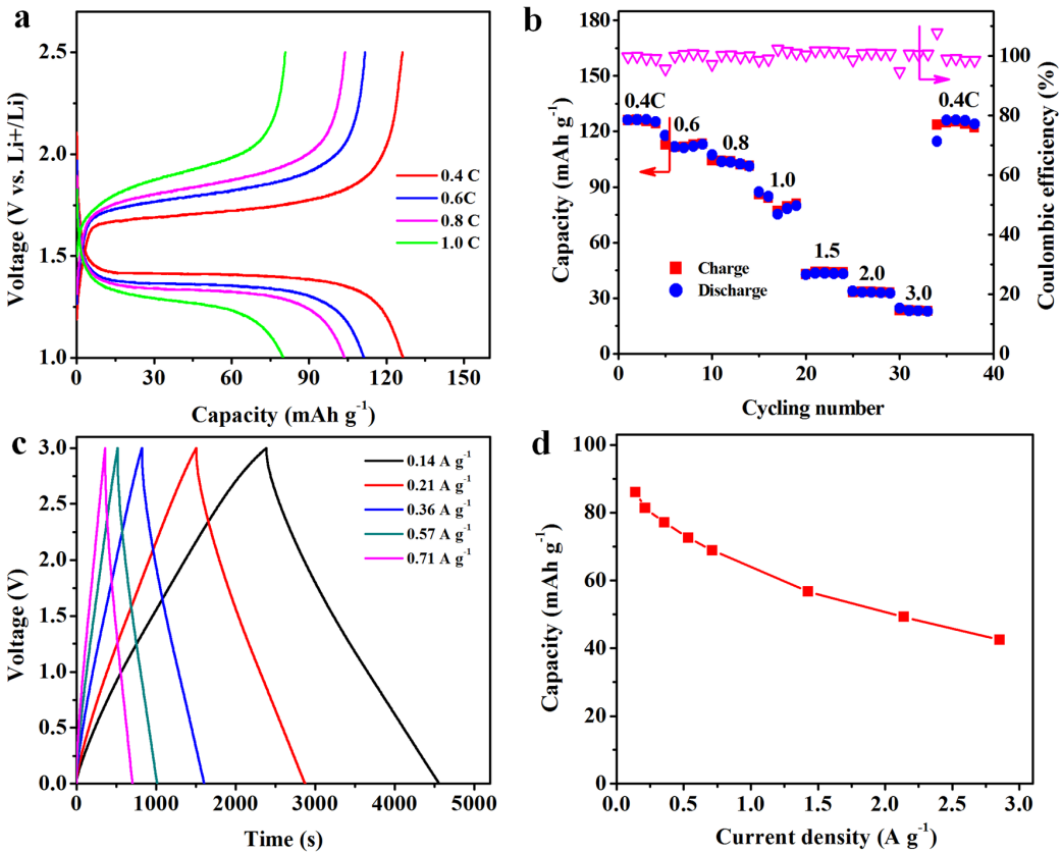

Fig. S6 Electrochemical performance of LTO nanospheres and nanoporous AG. (a) GCD profiles of LTO nanospheres from 0.2 to 2 C in 1M LiTFSI-P_{14}TFSI (1C=175 mA g^{-1}), displaying stable charge and discharge plateaus at around 1.55 V. (b) Specific capacity and coulombic effeciency of LTO nanospheres in 1M LiTFSI-P_{14}TFSI at various rates. (c) GCD curves of AG//AG-MSCs. (d) Specific capacity of AG at different current densities.

Specific capacity of AG is 85.9 mAh g^{-1}, while LTO has 102 mAh g^{-1}at the same current density of 0.14 A g^{-1} (0.8 C). According to the charge balance equation of $Q_-=Q_+$, or $m_-q_-=m_+q_+$ (Q: the capacity, and q: specific capacity), the ideal mass match ratio for LTO:AG was calculated to be 1.18, which is closed to 1. In this case, the evaluated mass match ratio of LTO:AG is 1.01 at current density of 0.21 A g^{-1}, corresponding to the electorde thickness of ~3 μm for LTO and ~10 μm for AG.

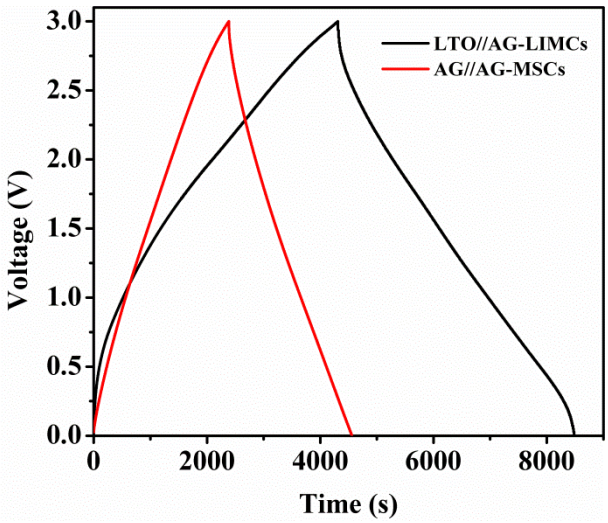

Fig. S7 GCD profiles of LTO//AG-LIMCs and AG//AG-MSCs at current density of 0.02 mA cm^{-2}. The longer discharge time of LTO//AG-LIMCs suggested higher specific capacitance than that of AG//AG-MSCs.

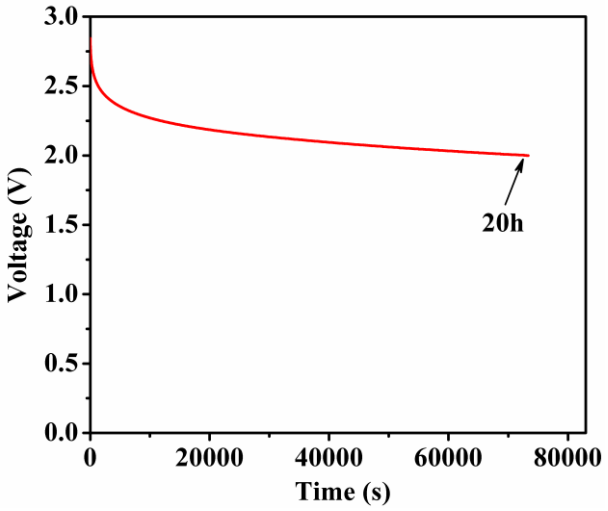

Fig. S8 Self-discharge curve of LTO//AG-LIMCs. The result presented that ASSP-LIMCs self-discharges in 20 h from V_{max} to 2/3 V_{max}, which is much superior to those of commercial supercapacitors from V_{max} to 1/2 V_{max}, such as a 3.5V/25mF commercial supercapacitor (8 h) and a 2.75V/44mF commercial supercapacitor (21 h).[4]

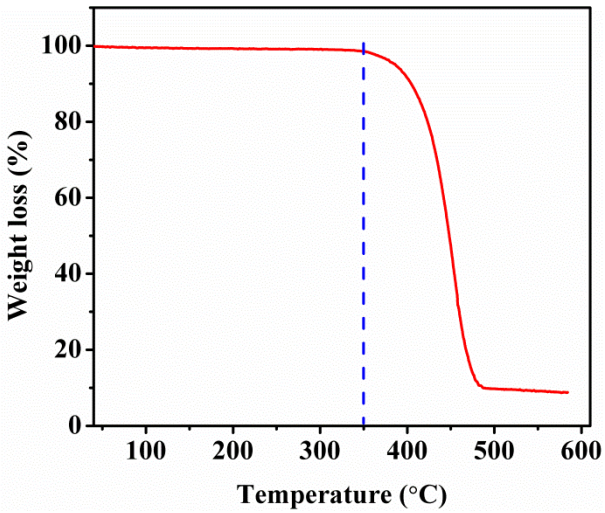

Fig. S9 TGA curve of the ionogel electrolyte of LiTFSI-P14TFSI-PVDF-HFP at N_2 atmosphere with a heating rate of 10 ^{o}C min^{-1}, showing that the ionogel electrolyte can be stable up to 350 ^{o}C.

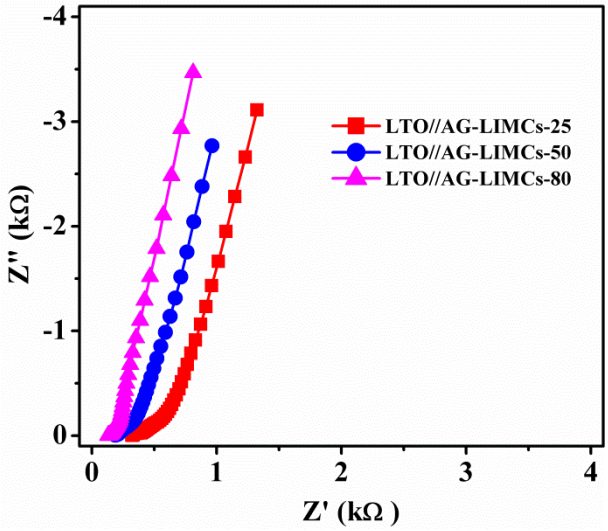

Fig. S10 Nyquist plots of LTO//AG-LIMCs at various temperatures (25, 50 and 80 ^{o}C).

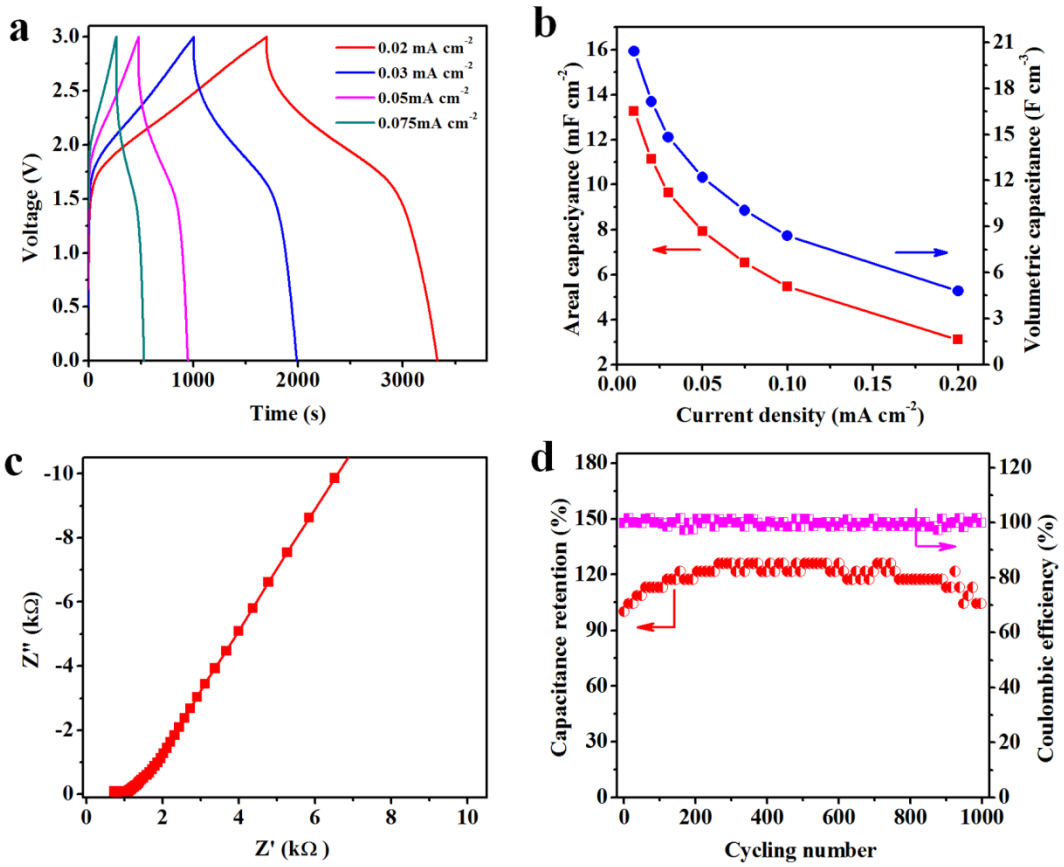

Fig. S11 Electrochemical performance of LTO//AG-LIMCs-0 tested at 0 °C. (a) GCD profiles of LTO//AG-LIMCs-0 at current densities from 0.02 to 0.075 mA cm^{-2}. (b) Areal capacitance and volumetric capacitance of LTO//AG-LIMCs-0 as a function of current density. (c) Electrochemical impedance spectrum and (d) cycling performance of LTO//AG-LIMCs-0, tested at 0.2 mA cm^{-2}.

It can be seen that LTO//AG-LIMCs-0 show the similar GCD curves to those of LTO//AG-LIMCs measured at higher temperatures (Fig. S11a). Due to the decrease of testing temperature, LTO//AG-LIMCs-0 at 0.01 mA cm^{-2} delivered a decreased areal capacitance of 13.3 mF cm^{-2} and volumetric capacitance of 20.4 F cm^{-3} (Fig. S11b), in comparison with those of LTO//AG-LIMCs at high temperatures (25, 50 and 80 °C, Fig. 3a). This result can be explained by larger equivalent series resistance of ~715 Ω and a smaller slope of LTO//AG-LIMCs-0 (Fig. S11c), due to the enlarged

viscosity and reduced Li-ion conductivity of ionogel electrolyte at 0 ^{o}C.[5-7] Notably, our LTO//AG-LIMCs-0 displayed good cycling performance without obvious degradation after 1000 cycles (Fig. S11d), an energy density of 25.5 mWh cm^{-3} and a robust power density of 1.3 W cm^{-3}.

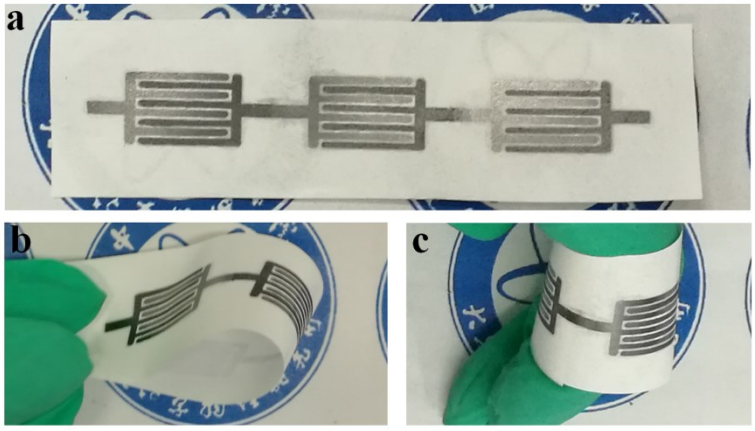

Fig. S12 Optical images of three serially-connected LTO//AG-LIMCs. (a-c) three serially-connected LTO//AG-LIMCs, showing flat (a), seriously bending (b), circle (c) states. Note that these tandem LTO//AG-LIMCs did not suffer from any structural disruption during different bending states.

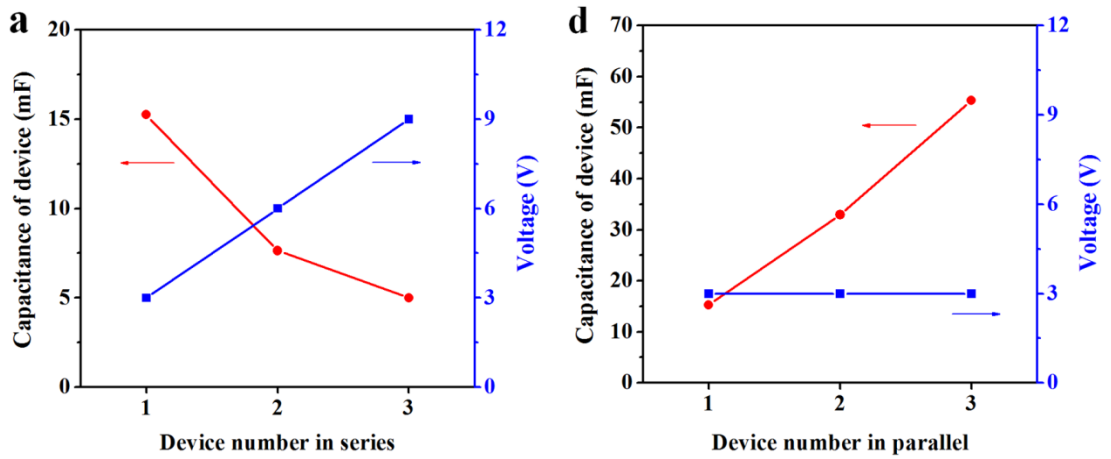

Fig. S13 Capacitance of LTO//AG-LIMCs in series and parallel. (a,b) Plot of capacitance and voltage *vs* device number in series (a) and in parallel (b).

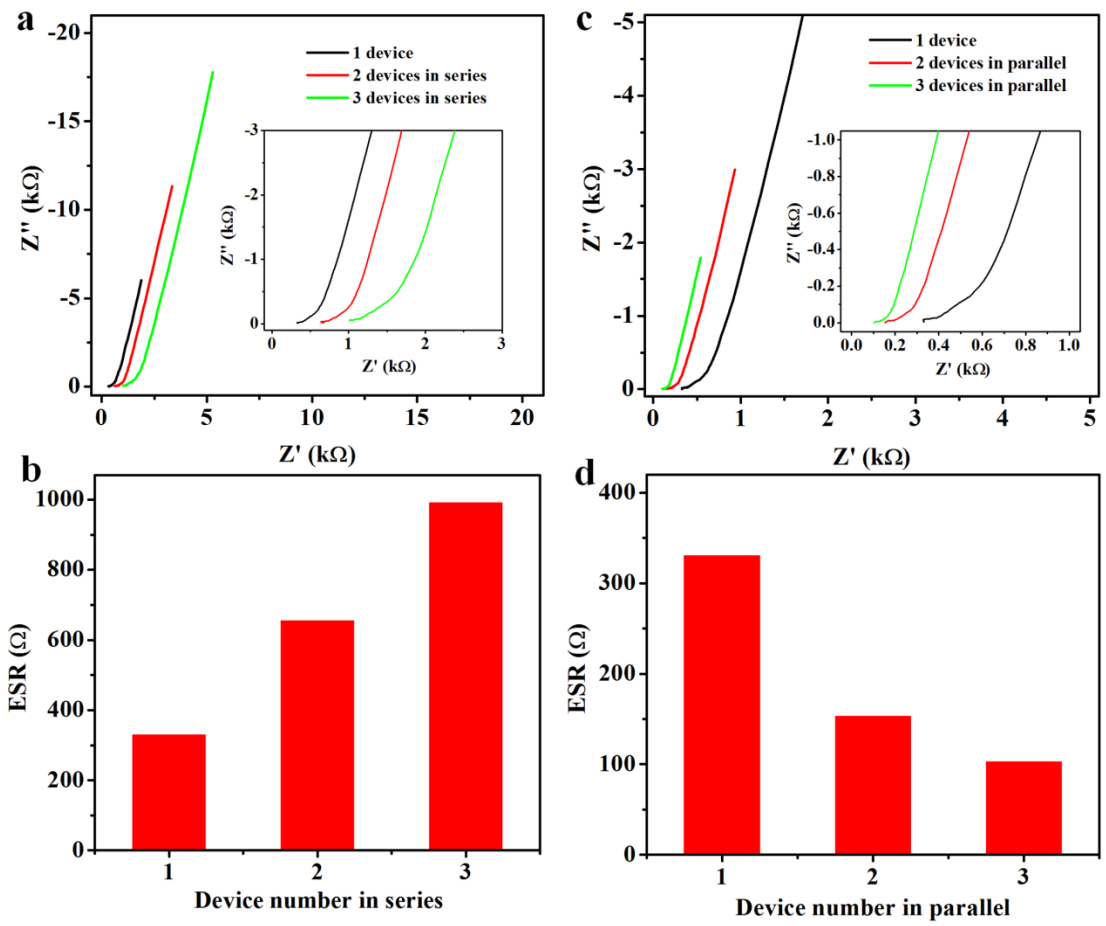

Fig. S14 EIS of LTO//AG-LIMCs connected in series and parallel. (a,b) EIS (a) of LTO//AG-LIMCs from 1 to 3 cells connected in series, showing the almost linear increase of ESR (b). (c,d) EIS (c) of LTO//AG-LIMCs from 1 to 3 cells connected in parallel, displaying a proportionally decreased ESR (d).

Table S1. Comparison of electrochemical performance of the state-of-the-art MSCs

MSCs	Tem (^{o}C)	Electrolyte	C_{device}^{areal} (mF cm^{-2})	$C_{device}^{volumetric}$ (F cm^{-3})	P_{device} (mW cm^{-3})	E_{device}(m Wh cm^{-3})	Refs
LTO//AG	RT	LiTFSI/P_{14}TFSI /PVDF-HFP	27.8	42.8	3460	53.6	This work
LTO//AG	0	LiTFSI/P_{14}TFSI /PVDF-HFP	13.3	20.4	1380	25.5	This work
LTO//AG	80	LiTFSI/P_{14}TFSI /PVDF-HFP	28.4	43.7	4620	54.6	This work
LTO//CNT	RT	1M $LiPF_6$/EC/ DEC	/	/	565	4.38	[8]
TP/EG	RT	PVA/H_2SO_4	0.85	81.5	~800000	11.3	[9]
rGO/TiO_2	RT	$EMIMNTF_2$	0.13	~12.7	~312000	~15.9	[10]
rGO/TiO_2	RT	PVA/H_2SO_4	0.36	~34.0	~82700	~4.8	[10]
LSG//LSG-MnO_2	RT	Na_2SO_4	~90	76	~10000	42	[11]
LIG-FeOOH// LIG-MnO_2	RT	PVA/LiCl	21.9	5.4	2891	2.4	[12]
GP/PANI-G/GP	RT	PVA/H_2SO_4	7.63	36.8	1140	3.1	[13]
EG//MP	RT	PVA/LiCl	3.60	14.6	1469	6.6	[13]
MXene/EG	RT	PVA/H_2SO_4	3.26	33	~800	3.5	[14]
MXene	RT	PVA/ H_2SO_4	27	357	15000	18	[15]
P2G3	RT	PVA/H_2SO_4	37.8	72.6	~3000	10.1	[16]
P2G3	RT	$EMIMBF_4$	26.5	53	~6500	46	[16]
Birnessite-MnO2	RT	Na_2SO_4	/	~230	295000	24.3	[17]
CoO/CNT	RT	PVA/KOH	/	17.4	/	3.5	[18]

CNT: carbon nanotube; TP: thiophene nanosheets; PVA: polyvinyl alcohol; rGO: reduced graphene oxide; $EMIMNTF_2$: 1-ethyl-3-methylimidazolium bis(trifluoromethylsulfonyl)imide; LIG: laser induced graphene; LPG: laser-processed graphene；EG: electrochemically exfoliated graphene; $BMIMPF_6$: 1-butyl-3-methylimidazolium hexafluorophosphate; GP: graphene/PH1000; PANI: polyaniline; MP: MnO_2 nanosheets/PH1000; $EMIMBF_4$: 1-ethyl-3-methylimidazolium tetrafluoroborate; MPG: methane plasma reduced graphene; P2G3: graphene-conducting polymer layers (2) and EG layers (3).

References

1 C. Wang, S. Wang, L. Tang, Y.-B. He, L. Gan, J. Li, H. Du, B. Li, Z. Lin and F. Kang, *Nano Energy*, 2016, **21**, 133-144.

2 Y. Zhu, S. Murali, M. D. Stoller, K. J. Ganesh, W. Cai, P. J. Ferreira, A. Pirkle, R. M. Wallace, K. A. Cychosz, M. Thommes, D. Su, E. A. Stach and R. S. Ruoff, *Science*, 2011, **332**, 1537-1541.

3 Z.-S. Wu, S. Yang, L. Zhang, J. B. Wagner, X. Feng and K. Müllen, *Energy Storage Mater.*, 2015, **1**, 119-126.

4 M. F. El-Kady and R. B. Kaner, *Nat. Commun.*, 2013, **4**, 1475.

5 Q. Zhou, P. D. Boyle, L. Malpezzi, A. Mele, J.-H. Shin, S. Passerini and W. A. Henderson, *Chem. Mater.*, 2011, **23**, 4331-4337.

6 M. Yamagata, Y. Matsui, T. Sugimoto, M. Kikuta, T. Higashizaki, M. Kono and M. Ishikawa, *J. Power Sources*, 2013, **227**, 60-64.

7 M. T. F. Rodrigues, G. Babu, H. Gullapalli, K. Kalaga, F. N. Sayed, K. Kato, J. Joyner and P. M. Ajayan, *Nat. Energy*, 2017, **2**, 17108.

8 W. Zuo, C. Wang, Y. Li and J. Liu, *Sci. Rep.*, 2015, **5**, 7780.

9 Z.-S. Wu, Y. Zheng, S. Zheng, S. Wang, C. Sun, K. Parvez, T. Ikeda, X. Bao, K. Müllen and X. Feng, *Adv. Mater.*, 2017, **29**, 1602960.

10 S. Wang, Z.-S. Wu, S. Zheng, F. Zhou, C. Sun, H.-M. Cheng and X. Bao, *ACS Nano*, 2017, **11**, 4283-4291.

11 M. F. El-Kady, M. Ihns, M. Li, J. Y. Hwang, M. F. Mousavi, L. Chaney, A. T. Lech and R. B. Kaner, *Pro. Natl. Acad. Sci. USA*, 2015, **112**, 4233-4238.

12 L. Li, J. Zhang, Z. Peng, Y. Li, C. Gao, Y. Ji, R. Ye, N. D. Kim, Q. Zhong, Y. Yang, H. Fei, G. Ruan and J. M. Tour, *Adv. Mater.*, 2016, **28**, 838-845.

13 X. Shi, Z.-S. Wu, J. Qin, S. Zheng, S. Wang, F. Zhou, C. Sun and X. Bao, *Adv. Mater.*, 2017, **29**, 1703034.

14 H. Li, Y. Hou, F. Wang, M. R. Lohe, X. Zhuang, L. Niu and X. Feng, *Adv. Energy Mater.*, 2017, **7**, 1601847.

15 Y.-Y. Peng, B. Akuzum, N. Kurra, M.-Q. Zhao, M. Alhabeb, B. Anasori, E. C. Kumbur, H. N. Alshareef, M.-D. Ger and Y. Gogotsi, *Energy Environ. Sci.*, 2016, **9**, 2847-2854.

16 Z. S. Wu, K. Parvez, S. Li, S. Yang, Z. Y. Liu, S. H. Liu, X. L. Feng and K. Müllen, *Adv. Mater.*, 2015, **27**, 4054-4061.

17 Y. Q. Li, X. M. Shi, X. Y. Lang, Z. Wen, J. C. Li and Q. Jiang, *Adv. Funct. Mater.*, 2016, **26**, 1830-1839.

18 Y. G. Zhu, Y. Wang, Y. Shi, J. I. Wong and H. Y. Yang, *Nano Energy*, 2014, **3**, 46-54.